

# Apertureless Scanning Near-Field Infrared Microscopy of a Rough Polymeric Surface

Boris B. Akhremitchev,<sup>†</sup> Steven Pollack,<sup>‡</sup> and Gilbert C. Walker<sup>\*,†</sup>

Department of Chemistry, University of Pittsburgh, G-12 Chevron Science Center, Pittsburgh, Pennsylvania 15260, and Department of Chemistry, Howard University, Washington, D.C. 20059

Received October 3, 2000. In Final Form: February 20, 2001

Infrared near-field microscopy using an apertureless probe technique has been accomplished to study the surface of a cast copolymer film. Two basic models for the predicted signal and the experimental data are presented. The first model includes plane wave light scattering by a conductive sphere and an infinitely wide absorptive layer placed on a semi-infinite conductor. This model shows infrared signal dependence on the layer absorption and predicts topographic coupling into the infrared signal. The experimental data also indicate that a significant component in the infrared contrast arises from the probe following the sample's topography, and a method to eliminate the influence of topography following is demonstrated. The images corrected by such a procedure show spatial resolution of approximately  $\lambda/80$ . A more complex model based on a three-dimensional finite difference time domain method was used to calculate scattering from a rough surface. Both constant tip-sample gap and constant tip-substrate height analyses were made, and it is found that constant height imaging is a preferred mode of operation. Calculations for dielectric and Lorentzian materials are reported. These calculations indicate that the near-field infrared signal attenuation for an absorptive object is larger than for a bare layer of the same thickness. This effect may be used to enhance chemical contrast in near-field imaging.

## Introduction

Scanning near-field microscopy provides optical resolution far beyond the diffraction limit of conventional microscopy.<sup>1</sup> It has been used to characterize samples ranging from semiconductors to polymers to biological materials using electromagnetic (EM) radiation from ultraviolet to radio waves (see refs 2 and 3 for recent reviews). The most common approach is to use the light emitted by a subwavelength aperture placed near the sample's surface as a light source and to detect the resulting EM radiation scattered, transmitted, or emitted by the sample.<sup>2</sup> This aperture probe approach usually provides  $\sim\lambda/20$  resolution in the visible part of the EM spectrum<sup>2</sup> and at best  $\lambda/10$  in the infrared<sup>4</sup> ( $\lambda$  is wavelength of light). An alternative technique employs a metallic, semiconductor, or dielectric probe as a local scatterer of EM radiation in the vicinity of the sample surface (this method was proposed by Wessel<sup>5</sup> in 1985; for original experimental implementations, see refs 6–8). This approach has been used to detect local scattering<sup>9–11</sup> as well as one- and two-photon fluorescence from beneath the probe.<sup>12</sup> Apertureless imaging usually provides resolution

superior to the apertured probe approach, and the limitation of the probe transmission bandwidth is circumvented. Resolution exceeding  $\lambda/100$  in the visible<sup>9</sup> and  $\lambda/300$  in the infrared<sup>13</sup> has been reported. Radiation scattered by the sample is affected by the local optical properties of the sample and by the geometry of the probe-sample assembly.<sup>1</sup> EM radiation at the surface of an inhomogeneous sample varies according to the sample's properties. When scattered radiation propagates away from the sample, high spatial frequency components decay, resulting in the well-known resolution limit of far-field microscopy.<sup>1</sup> When a small scattering object is placed near the sample, it converts some of the decaying high-frequency components of the scattered radiation into the propagating field. Such propagating radiation can be detected by means of far-field optics, and variation in the detected signal as a function of the probe position along the surface provides a map of the near-field region, caused by optical properties of the surface.<sup>14</sup> For rough samples, surface topography affects the local field distribution, modulating the detected signal.<sup>15,16</sup> Separation of the optical contrast from the topographic effects is a primary

<sup>†</sup> University of Pittsburgh.

<sup>‡</sup> Howard University.

(1) Courjon, D.; Bainier, C. *Rep. Prog. Phys.* **1994**, *57*, 989.

(2) Hecht, B.; Sick, B.; Wild, U. P.; Deckerd, V.; Zenobi, R.; Martin, O. J. F.; Pohl, D. W. *J. Chem. Phys.* **2000**, *112*, 7761.

(3) Buratto, S. K. *Curr. Opin. Solid State Mater. Sci.* **1996**, *1*, 485.  
Dunn, R. C. *Chem. Rev.* **1999**, *99*, 2891. Barbara, P. F.; Adams, D. M.; O'Connor, D. B. *Annu. Rev. Mater. Sci.* **1999**, *29*, 433. McNeill, J. D.; O'Connor, D. B.; Barbara, P. F. *J. Chem. Phys.* **2000**, *112*, 7811. van Hulst, N. F.; Veerman, J.-A.; Garca-Parajo, M. F.; Kuipers, L. (Kobus) *J. Chem. Phys.* **2000**, *112*, 7799.

(4) Dragnea, B.; Preusser, J.; Schade, W.; Leone, S. R.; Hinsberg, W. D. *J. Appl. Phys.* **1999**, *86*, 2795.

(5) Wessel, J. *J. Opt. Soc. Am. B* **1985**, *2*, 1538.

(6) Zenhausern, F.; O'Boyle, M. P.; Wickramasinghe, H. K. *Appl. Phys. Lett.* **1994**, *65*, 1623.

(7) Inouye, Y.; Kawata, S. *Opt. Lett.* **1994**, *19*, 159.

(8) Bachelot, R.; Gleyzes, P.; Boccara, A. C. *Microsc., Microanal., Microstruct.* **1994**, *5*, 389.

(9) Zenhausern, F.; Martin, Y.; Wickramasinghe, H. K. *Science* **1995**, *269*, 1083. Hamann, H. F.; Gallagher, A.; Nesbitt, D. J. *Appl. Phys. Lett.* **1998**, *73*, 1469. Hubert, C.; Levy, J. *Appl. Phys. Lett.* **1998**, *73*, 3229. Gresillon, S.; Cory, H.; Rivoal, J. C.; Boccara, A. C. *J. Opt. A: Pure Appl. Opt.* **1992**, *1*, 178.

(10) Adam, P. M.; Royer, P.; Laddada, R.; Bijeon, J. L. *Ultramicroscopy* **1998**, *71*, 327. Yamaguchi, M.; Sasaki, Y.; Sasaki, H.; Konada, T.; Horikawa, Y.; Ebina, A.; Umezawa, T.; Horiguchi, T. *J. Microsc. (Oxford)* **1999**, *194*, 552.

(11) Sasaki, H.; Sasaki, Y. *J. Appl. Phys.* **1999**, *85*, 2026.

(12) Azoulay, J.; Debarre, A.; Richard, A.; Tchenio, P. *J. Microsc. (Oxford)* **1999**, *194*, 486. Sanchez, E. J.; Novotny, L.; Xie, X. S. *Phys. Rev. Lett.* **1999**, *82*, 4014.

(13) Lahrech, A.; Bachelot, R.; Gleyzes, P.; Boccara, A. C. *Appl. Phys. Lett.* **1997**, *71*, 575. Knoll, B.; Keilmann, F. *J. Microsc. (Oxford)* **1999**, *194*, 512.

(14) Knoll, B.; Keilmann, F. *Nature* **1999**, *399*, 134.

(15) Hecht, B.; Bielefeldt, H.; Inouye, Y.; Pohl, D. W.; Novotny, L. *J. Appl. Phys.* **1997**, *81*, 2492.

(16) Martin, O. J. F. *J. Microsc. (Oxford)* **1999**, *194*, 235.

concern in understanding the near-field optics. This separation is complicated by the influence of the local probe on the near field.<sup>17</sup> Theoretical models are necessary to calculate the local field distribution near such topographic objects and to predict the signal resulting from the light interaction with the probe-sample system.<sup>18</sup>

We aim to understand the structure and dynamics of polymer interfaces on the nanoscale.<sup>19</sup> In this paper, we apply apertureless infrared scanning near-field microscopy to study a thin film of polystyrene-poly(dimethylsiloxane) (PS-PDMS) diblock polymer that was spin-cast onto metal. An oscillating metallic probe is used as a light scatterer. The map of the scattered infrared signal has high correlation with topographic features of the polymer film. This correlation depends on imaging conditions, and in certain cases the sign of the correlation can be reversed. We describe a procedure for eliminating such correlation from the collected signal. We use two theoretical models to describe our experimental setup. One simple theoretical model computes the scattering by a small conductive sphere found near a layer of an absorbing dielectric placed on a semi-infinite conductor. This model predicts a correlation of the scattered signal with the sample's topography, but it lacks the desired spatial resolution. To calculate the imaging properties of our microscope, we apply the three-dimensional finite difference time domain (FDTD) method<sup>20,21</sup> to solve Maxwell equations to calculate the scattering for an arbitrary probe-sample geometry. FDTD has been successfully used in the past to model near-field signals for aperture<sup>22,23</sup> as well as apertureless probe<sup>11,24</sup> techniques.

This paper is organized as follows: First, we describe our experimental setup and theoretical models. Next, we discuss experimental data and the results of calculations. The paper finishes with conclusions.

### Experimental Setup

Our near-field microscope utilizes the scanning capabilities of a commercial atomic force microscope (Multimode AFM, Digital Instruments, Santa Barbara, CA). Figure 1 shows the scheme of the apparatus. The infrared light emitted by a carbon dioxide laser (wavelength approximately  $10\ \mu\text{m}$ ) is focused by a parabolic mirror onto the end of a tungsten-coated cantilever probe<sup>14</sup> perpendicular to the long axis of the probe. We use *p*-polarized light with a  $73^\circ$  angle of incidence. The spot size is approximately  $100\ \mu\text{m}$ , and the radiation power is 20–100 mW. The probe is a commercial silicon probe (Silicon MDT, Moscow, Russia) coated with 25 nm of tungsten. The probe characteristics are length 130  $\mu\text{m}$ , width 35  $\mu\text{m}$ , resonance frequency 150 kHz, and radius of curvature of the tip 35 nm. These probe parameters are given as specified by the manufacturer. Driving the probe near its resonance frequency excited mechanical oscillation of the probe (100–200 nm total amplitude). Imaging of the surface of the sample in intermittent-contact (tapping) mode was performed simultaneously with the detection of the scattered infrared signal. An infrared-transparent multimode optical fiber (500  $\mu\text{m}$  chal-

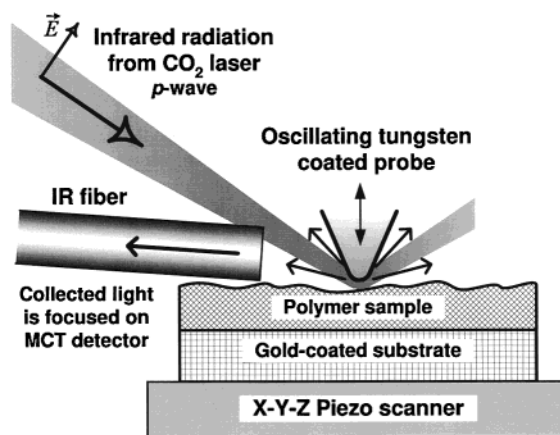


**Figure 1.** This diagram illustrates the modification of the tapping mode scanning AFM into an apertureless near-field scanning infrared microscope.

cogenide glass core) was placed near the probe ( $\sim 0.5\ \text{mm}$  away) to collect light scattered at a small angle to the surface of the sample in the direction opposite to the incident beam (see Figure 1). The fiber is slightly shifted sideways and tilted in the horizontal direction to allow propagation of the incident radiation. The positioning was restricted to a significant extent by the geometry of the commercial AFM used in our experiments. Light emitted from the optical fiber was focused onto a MCT infrared detector (Graseby Infrared, Orlando, FL). The electrical signal from the detector was amplified by a lock-in amplifier (SR844, Stanford Research Systems, Sunnyvale, CA) at the frequency of the cantilever oscillation and collected by a computer simultaneously with AFM data. The use of an oscillating cantilever eliminated the dc background signal<sup>10</sup> and provided the benefits of sensitive lock-in detection. Our setup is similar to the apparatus described in ref 25, which, in contrast to ours, operates in the visible wavelength region.

The polymer film sample was prepared by spin-casting a 1.5 mg/mL solution of polystyrene-poly(dimethylsiloxane) diblock polymer<sup>26</sup> in  $\text{CH}_2\text{Cl}_2$  at 3000 rpm using a Headway Research ED101 photo resist spinner. The molecular weight of the polymer was 144 kDa with 1:2.3 PDMS/PS mole ratio.<sup>26</sup> A gold-coated microscope coverslip was used as the substrate to reflect infrared radiation and avoid excessive heating of the AFM piezo scanner.

### Theoretical Models

To predict the dependence of the scattered signal on imaging conditions, we first devise a simple analytical model consisting of a plane electromagnetic wave incident on a scattering probe and an infinitely wide absorptive layer placed on a semi-infinite conductor. Scattering from the probe is calculated using a model for scattering by a small conductive sphere. Scattering from such a probe consists of fields emitted by magnetic and electric dipoles, placed at the middle of the sphere.<sup>27</sup> The boundary conditions for the electric vector at the surface of the perfect conductor allow us to further simplify the model by replacing the perfect conductor with a mirror image of the absorptive layer, scattering probe, and incident wave. The electric vector at the registration point is calculated as a sum of the electric vectors due to scattering of the original plane wave, the attenuated and phase shifted wave propagating through the layer of the sample, and mirror images of those plane waves by two probes. Spherical components ( $r, \theta, \phi$ ) of the electric vector of

(17) Bozhevolnyi, S. I. *J. Microsc. (Oxford)* **1999**, *194*, 561.

(18) Dereux, A.; Girard, C.; Weeber, J.-C. *J. Chem. Phys.* **2000**, *112*, 7775.

(19) Akhremitchev, B. B.; Mohny, B. K.; Marra, K. G.; Chapman, T. M.; Walker, G. C. *Langmuir* **1998**, *14*, 3976. Akhremitchev, B. B.; Walker, G. C. *Langmuir* **1999**, *15*, 5630. Bemis, J. E.; Akhremitchev, B. B.; Walker, G. C. *Langmuir* **1999**, *15*, 2799.

(20) Yee, K. S. *IEEE Trans. Antennas Propag.* **1966**, *AP-14*, 302.

(21) Taflov, A. *Computational electrodynamics: the finite-difference time-domain method*; Artech House: Boston, 1995.

(22) Bian, R. X.; Dunn, R. C.; Xie, X. S.; Leung, P. T. *Phys. Rev. Lett.* **1995**, *75*, 4772. Kann, J. L.; Milster, T. D.; Froehlich, F. F.; Ziolkowski, R. W.; Judkins, J. B. *J. Opt. Soc. Am. A* **1995**, *12*, 1677. Vasilyeva, E.; Taflov, A. *Opt. Lett.* **1998**, *23*, 1155. Chavez-Pirson, A.; Chu, S. T. *J. Microsc. (Oxford)* **1999**, *194*, 421.

(23) Furukawa, H.; Kawata, S. *Opt. Commun.* **1996**, *132*, 170.

(24) Furukawa, H.; Kawata, S. *Opt. Commun.* **1998**, *148*, 221.

(25) Wurtz, G.; Bachelot, R.; Royer, P. *Rev. Sci. Instrum.* **1998**, *69*, 1735.

(26) Pollack, S. K.; Singer, D. U.; Morgan, A. M. *Polym. Prepr. (Am. Chem. Soc., Div. Polym. Chem.)* **1999**, *40*, 370.

(27) Jackson, J. D. *Classical electrodynamics*; John Wiley & Sons: New York, 1975; pp 411–418.

Chart 1

$$\vec{E}_{sc}(r, \theta, \phi) = \frac{k^2 a^3 e^{ikr}}{2r} \begin{pmatrix} 0 \\ E_x^{inc} \cos\phi(2\cos\theta - \sin\alpha) + E_y^{inc} \sin\phi(2\cos\theta - \sin\alpha) - E_z^{inc}(2\sin\theta + \cos\phi\cos\alpha) \\ E_x^{inc} \sin\phi(-2 + \cos\theta\sin\alpha) + E_y^{inc}(\cos\phi(2 - \cos\theta\sin\alpha) + \sin\theta\cos\alpha) + E_z^{inc} \cos\theta\sin\phi\cos\alpha \end{pmatrix}$$

scattered radiation were calculated using the equation found in Chart 1, where  $E^{inc}$  are Cartesian components of the electric vector of the incident plane wave,  $k$  is the magnitude of the wavevector,  $a$  is the radius of the sphere,  $\alpha$  is the angle between the wavevector and the surface, and  $r$  is the distance between the observation point and the origin. When the conductive sphere is shifted from the origin, the scattered field is calculated by transforming the coordinate system. We averaged intensity  $|E_{sc}|^2$  over a range of angles  $\theta$  and  $\phi$  in order to simulate the light collected in the experiment. Calculations were performed as a function of probe separation from the surface. Because in the experiment we collected the ac component while dithering the probe in a direction perpendicular to the surface, the calculated signal was differentiated with respect to the separation variable. These calculations provide the distance and absorption dependence of the scattered signal.

To calculate the scattering signal for samples with topographic features on the surface, we use the finite difference time domain method. In our implementation, FDTD solves the Maxwell curl equations for isotropic nonmagnetic media on a three-dimensional grid by propagating electromagnetic fields through the calculation space. We use the FDTD algorithm according to ref 21. Scattered fields in the far field are calculated by using frequency domain near-field to far-field transformation.<sup>28</sup> The scattered signal measured in the experiment is computed by integrating the intensity of the calculated scattered signal in the direction of detection.

In FDTD calculations, dielectric and absorptive objects are placed on the surface of a perfect conductor, and a conductive scattering probe is placed nearby and scanned across the surface. At each lateral position of the probe, we calculate the scattered signal at different probe-sample separations to obtain the ac component of the scattering signal. Probe scanning can be performed at two modes: constant height above the perfect conductor interface or constant probe-sample gap. Figure 2 shows the geometry of the three-dimensional model used in our FDTD calculations.

## Results and Discussion

**Experiment.** We used a scratch test followed by AFM height imaging to determine the thickness of the polymer film. The thickness of the film was approximately  $1.0 \mu\text{m}$  in the area where the near-field images were collected. Topographic images of the sample revealed that ringlike structures have formed on the surface of the sample (Figure 3). These rings are characterized by  $\sim 500 \text{ nm}$  external diameter and  $\sim 250 \text{ nm}$  internal diameter and are  $\sim 20 \text{ nm}$  high. The formation of ringlike structures during solvent evaporation has been observed for many materials; see for example the paper by Hahm and Sibener,<sup>29</sup> describing this phenomenon for polystyrene-*b*-poly(methyl methacrylate). The cantilever oscillation phase signal collected simultaneously with the topography shows that the phase shift response is different on the

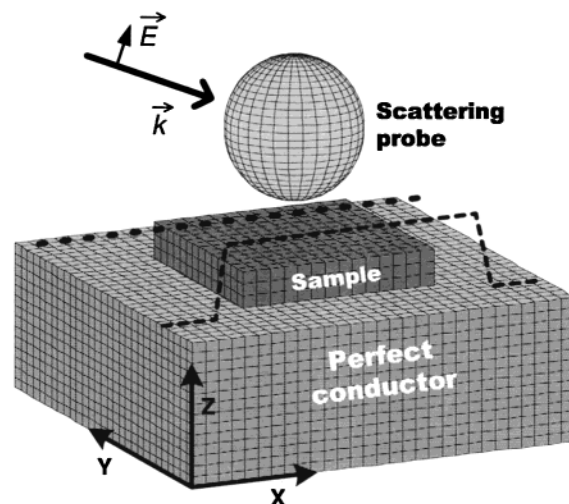


**Figure 2.** Figure demonstrates the geometry used in FDTD calculations. The scattering probe scans above the interface. Dashed lines indicate possible scanning trajectories: at a constant height above the conductor or at a constant probe-sample gap.

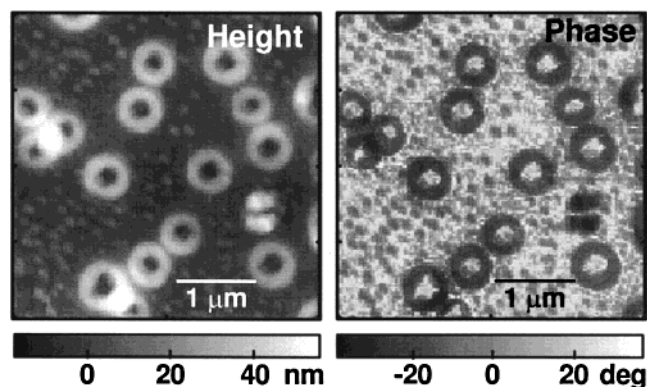


**Figure 3.** Tapping mode AFM maps of the PS-PDMS sample topography and cantilever phase shift show the presence of ringlike structures on the surface of the polymer film. Phase contrast usually arises from variations in the elasticity in the sample and is often attributed to differences in chemical composition of the sample.

rings than on the relatively flat surrounding area. The origin of the phase contrast could be due to varying chemical composition of the rings as well as due to larger compressibility of the rings that protrude from the sample.<sup>30</sup> A scattered infrared signal modulated by the oscillating probe (henceforth "infrared signal") was collected using the  $982 \text{ cm}^{-1}$  radiation of a  $\text{CO}_2$  laser. At this frequency, the PDMS component of the polymer has a noticeable absorption, in contrast to the PS block. Therefore, the difference in scattered signal from the rings versus the flat area might be taken to indicate a sample chemical composition difference.<sup>14,4</sup> A map of the infrared signal collected simultaneously with the topographic map is shown in Figure 4. Images were collected during intermittent-contact scanning of the surface, with the cantilever

(28) Maloney, J. G.; Smith, G. S. In *Advances in computational electrodynamics: the finite-difference time-domain method*; Taflov, A., Ed.; Artech House: Boston, 1998.

(29) Hahm, J.; Sibener, S. J. *Langmuir* **2000**, *16*, 4766.

(30) Magonov, S. N.; Reneker, D. H. *Annu. Rev. Mater. Sci.* **1997**, *27*, 175.

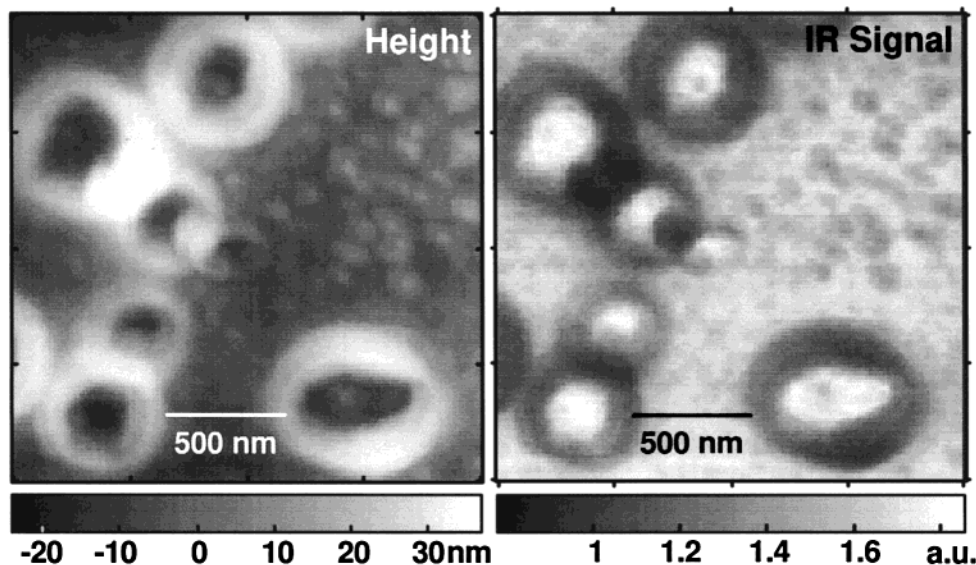


**Figure 4.** Topography and infrared signals collected simultaneously. The scanned area is adjacent to the area in Figure 4. Data were collected using 50 mW of infrared radiation ( $982\text{ cm}^{-1}$ ) focused onto the cantilever by a parabolic mirror. The cantilever oscillation amplitude was 200 nm at 180 kHz. The ratio of the ac to dc signal on the MCT infrared detector was  $\sim 5 \times 10^{-4}$ . The detected ac component is  $\sim 10^{-7}$  of the incident radiation power. High correlation between topography and scanning near-field, present on the maps here, is often thought to result from constant-gap scanning of topographic features.

oscillating at 180 kHz with 200 nm peak-to-peak amplitude. Topographical, protruding ringlike structures exhibit large variations in the associated infrared signals, with signal modulation up to  $\sim 20\%$  compared to flat area signals. There is a high correlation between the two images, which is thought to be a result of constant-gap scanning of nonflat objects<sup>15,31</sup> (see below). The signal dependence on the distance from the sample surface shows a fast decay close to the sample's surface (Figure 5, upper graph), which is followed by a nonmonotonic dependence (see inset in the graph). The magnitude of the scattered signal presented in these graphs is scaled to the cantilever oscillation amplitude, which was decreasing upon approach to the sample. Separate tests indicated that at fixed sample-probe distances the scattered signal is directly proportional to the cantilever amplitude (data not shown). Additionally, we have collected the dependence of the infrared signal map on the mean separation between the probe and the sample. During scanning, after each scan line, which probes the topography of the sample, we can lift the probe and repeat the probe trajectory at a desired gap above the sample. Infrared signal images collected at two different gap values above the sample are presented in Figure 5, lower graphs. There is an obvious contrast reversal on these two images, indicating that negative contrast on ringlike structures when the probe is close to the sample comes from the dependence of scattered light interference on the probe position, modulated by the topography of the sample. Contrast reversal and nonmonotonic distance dependence are also described in ref 32 for aperture probe imaging at visible wavelengths. Interference patterns were detected on the slopes of polystyrene droplets on a flat coverslip substrate using transmission aperture probe imaging at 488 nm by Goldner et al.<sup>33</sup> Apertured probe studies in the infrared of the subwavelength polystyrene particles on a calcium fluoride substrate also indicate that the signal detected

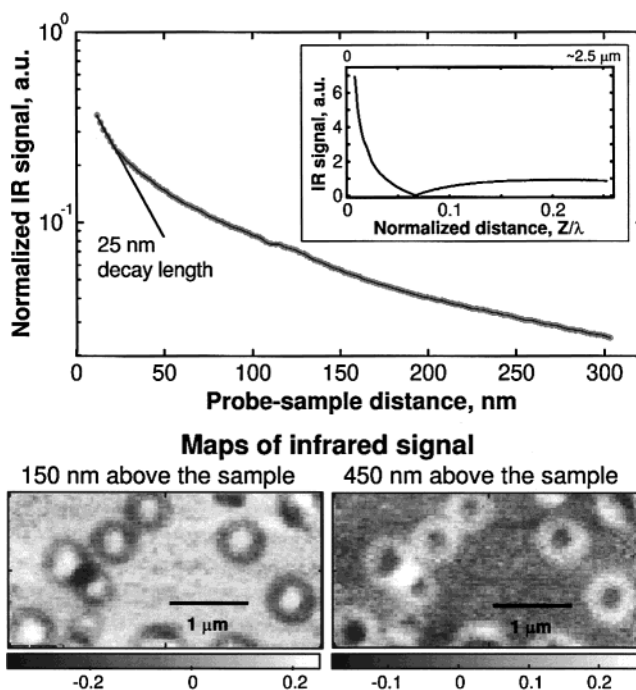


**Figure 5.** Distance dependence of the infrared signal. The top panel shows that the IR signal decays rapidly near the surface of the sample. The inset in the graph includes the signal collected over a longer distance, where the infrared signal does not decay monotonically with distance. Infrared signal maps collected at different probe-sample distances exhibit a reversal of the contrast in the infrared signal. This supports the hypothesis that a significant component of contrast in the infrared image arises from the scanning probe following the topography.

in transmission is strongly coupled to the sample's topography.<sup>34</sup> We note that in our case, according to the distance dependence of the IR signal, at some distance above the sample surface the signal increases with increasing the distance. Therefore, tall topographic structures of the sample will exhibit higher signals and image contrast will be reversed.

(31) Knoll, B.; Keilmann, F.; Kramer, A.; Guckenberger, R. *Appl. Phys. Lett.* **1997**, *70*, 2667.

(32) Weston, K. D.; Buratto, S. K. *J. Phys. Chem. B* **1997**, *101*, 5684.

(33) Goldner, L. S.; Hwang, J.; Bryant, G. W.; Faselka, M.; Absil, P. P.; Hryniewicz, J. V.; Johnson, F. G.; Shen, H.; Ho, P.-T. *Appl. Phys. Lett.* **2001**, *78*, 583.

(34) Palanker, D. V.; Simanovskii, D. M.; Huie, P.; Smith, T. I. *J. Appl. Phys.* **2000**, *88*, 6808.

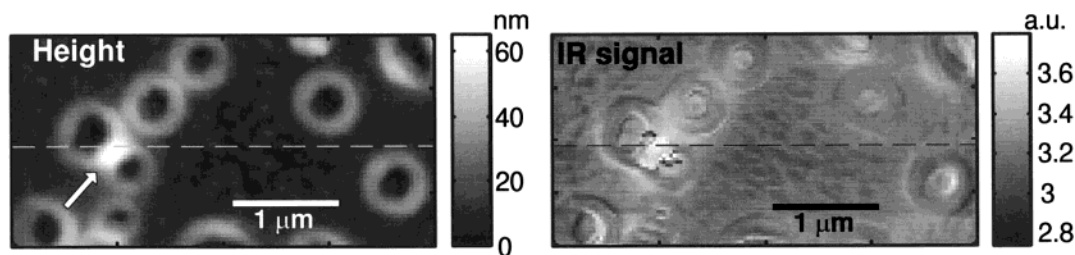


**Figure 6.** Infrared signal image created by elimination of topography-following coupling into the near-field signal. The contrast from topographic structures is mostly removed; the residual differential signal on the edges probably remains because of a slight drift in the images used for interpolation. Dashed lines indicate the position for the data shown in Figure 7.

As indicated in Figure 3, scanning above different areas of the sample modifies the cantilever oscillation phase. To avoid having this phase modulation influence the IR signal, we detect the total amplitude of IR modulation at the cantilever oscillation frequency. For cantilever oscillation amplitudes that are small compared to the wavelength of IR radiation, the detected signal depends linearly on the cantilever amplitude. During image scanning, the cantilever amplitude is slightly modulated by topographic features of the sample. This modulation was well below 0.5% of the total cantilever amplitude, and it has differential character in the direction of scanning (data not shown). Maps of our IR signal were uncorrelated to maps of cantilever amplitude changes, and we neglect this effect in the analysis of our data.

To exclude topographic contributions into our infrared signal, one needs to perform scanning above the surface *without* following the topography.<sup>15,35</sup> Our instrument does not have such a mode of imaging; therefore, we used another approach.<sup>36</sup> We collected seven topographic and infrared signal maps at different probe–surface gap values, from 27 to 104 nm, which gives us the three-dimensional signal dependence.<sup>37</sup> This range was large enough so we could interpolate our infrared signal to a plane above the surface. The results of interpolation are presented in Figure 6. For comparison, we show the sample's topography on the upper image and the interpolated infrared signal on the lower image. Almost all contrast found on the rings was eliminated, with some residual signal on the sides. A noticeable positive signal remains in the area where the rings intercept, and a small negative signal is noticeable in the flat area between the rings in the middle of the image. When we perform an interpolation of our data, the protrusion on the surface (indicated by the white arrow on the upper image of Figure 6) is closer to the interpolating plane than the rest of the surface. Therefore, the positive signal in Figure 6B could be a result of such proximity (FDTD calculations support this hypothesis; see below). Constant-height scanning measurements above a polystyrene particle using IR transmission aperture imaging<sup>34</sup> also show an increase of the near-field signal when the probe is placed above the particle. The top panel of Figure 7 shows constant-gap data for one scan line (indicated with dashed lines in Figure 6). The corresponding constant-height mode signal is given in the middle panel, and the topography is shown in the lower panel. The decrease in the amplitude of the bright spot mentioned above provides us with the resolution of our apertureless microscope, approximately 125 nm ( $\sim\lambda/$

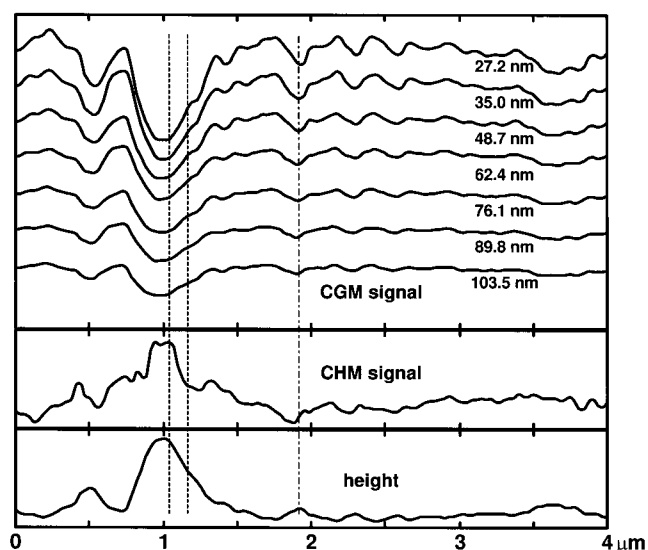


**Figure 7.** The figure provides data collected at different gap values and illustrates the interpolation procedure. The constant-gap signals are shown on the top panel. Numbers labeling the curves indicate the gap size. The middle panel gives the interpolated constant-height signal for the same scan line. On the lower panel, topography is shown for comparison.

80), as indicated by dashed vertical lines on the figure. We note that this value is larger than the distance from the surface to the plane where the signal was interpolated ( $\sim 70$  nm).

Small, negative contrast features are discernible in the relatively flat center of the image in Figure 6B, where there should be no contrast-modulating mechanism as found for the large protruding feature in the interpolated infrared signal.<sup>23</sup> Figure 7 shows that there is an obvious decrease in the signal amplitude as the distance from the sample increases for both high topographic features and small features on a flatter area (one such feature is indicated with a dashed–dotted vertical line). However, in the case of small features, the contrast does not reverse upon interpolation. This indicates that this negative contrast arises because of local variations of optical properties, namely, because of light absorption by the PDMS block of the polymer. This suggestion is supported by the known surface segregation in spin-cast films of PS–PDMS diblock copolymers.<sup>38</sup> The surface coverage by PDMS is not complete for a 0.3 mole fraction PDMS block, which might explain observed patches.<sup>38</sup> In comparison, the constant-height mode images of ringlike structures indicate that those structures are similar in chemical composition compared to other areas of the sample, which contradicts a trivial and obviously incorrect interpretation of the phase imaging data, shown in Figure 3.

(35) Novotny, L.; Hecht, B.; Pohl, D. W. *Ultramicroscopy* **1998**, *71*, 341.

(36) Hatano, H.; Inouye, Y.; Kawata, S. *Opt. Lett.* **1997**, *22*, 1532. Jordan, C. E.; Stranick, S. J.; Richter, L. J.; Cavanagh, R. R. *J. Appl. Phys.* **1999**, *86*, 2785.

(37) Levy, J.; Cohen, A.; Awschalom, D. D. *Rev. Sci. Instrum.* **1995**, *66*, 3385.

(38) Chen, X.; Gardella, J. A. *Macromolecules* **1992**, *25*, 6621.

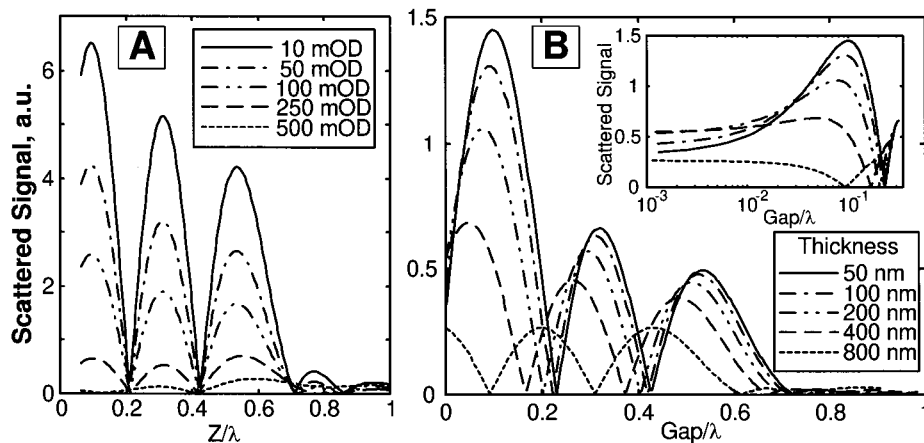


**Figure 8.** This figure presents calculations using the homogeneous and flat layer mode. The distance dependence of infrared signals for a layer of constant thickness and different absorption values is plotted in panel A. The graphs present an oscillating nonperiodic function of distance, with amplitudes decreasing when layer absorption is increasing. Panel B shows the calculated signal for different thicknesses of the layer characterized by a constant absorption coefficient, as a function of scattering probe height above the surface of the layer. This simulates constant-gap scanning and predicts topographic coupling into the infrared signal. The parameters of the calculations are given in the text.

**Theory.** We have calculated the infrared signal using our analytical dipole-probe model for two cases. First, for constant layer thickness and different values of layer absorption we calculate the signal dependence on distance between the spherical probe and the conductor. Second, for different thicknesses of the layer characterized by a constant absorption coefficient, we compute the dependence of the infrared signal on the probe separation from the layer surface. In these calculations, the EM wave is *p*-polarized (electric field is in the plane of incidence), the angle of incidence is  $75^\circ$ , the sphere size is 100 nm, the real part of the layer refractive index is 1.4, and the radiation wavelength is  $10\ \mu\text{m}$ . Panel A of Figure 8 gives the distance dependence of the infrared signal for a 500 nm thick layer, with different values of total layer absorption, as indicated on the graph. This calculation predicts that the distance dependence of the signal is not monotonic, with the first minimum at approximately  $\lambda/4$ , and that the signal decreases with increasing absorption. The absorption dependence of the scattered signal provides for chemical specificity for this kind of scanning probe technique. We used similar calculations to predict the probe-sample separation at which the infrared signal is at a minimum, as shown on the upper panel of Figure 5. For a film  $1.0\ \mu\text{m}$  thick and with a 1.45 index of refraction,<sup>34</sup> the calculated minimum occurs at the gap (gap size normalized to IR wavelength) of 0.057, which is surprisingly close to the experimental value of 0.067, considering approximations made in the above model (the error is 1% of the wavelength). Calculations of the IR signal using a fixed value of the absorption coefficient (we use a value of 200 mOD/ $\mu\text{m}$ ) and varying the sample's thickness as a function of probe-surface separation are plotted on panel B of Figure 8. For a constant tip-sample gap (which is a typical condition for AFM imaging), we see an obvious layer thickness dependence of the signal. This means that collecting an infrared signal on a sample with a varying thickness will also produce a topology-related signal. The inset in panel B shows the same dependence for small tip-sample separations. Here, we see that changing the layer thickness from 100 to 200 nm might result in a negative or positive change of the infrared signal, depending on the probe-sample gap. This is another clear indication that flatter samples are better suited for near-field imaging. Contrast reversal at different probe heights above the surface, described in the preceding experimental

section, is probably caused by this kind of interference effect. In general, we expect that topographic coupling into the near-field signal in constant-gap mode is not limited to the case of a conductive probe at a conductive interface but will be present for other polarizable materials.

The model used above provides qualitative information about the infrared signal generated by our near-field microscope. It captures the nonmonotonic signal change with increasing probe-sample separation, observed in the experiment (Figure 5). However, this model neglects multiple scattering effects and fails to predict the experimentally observed steep increase in the scattered field as the probe approaches the surface. In addition, it cannot be used to calculate the imaging properties of our instrument because the sample objects are assumed to be infinite in lateral dimensions. Therefore, we now proceed to numerical calculations with the FDTD method that were used for more realistic calculations of the infrared signal to predict signals arising from the scanning of heterogeneous samples.<sup>11</sup> In all of these calculations, *p*-polarized radiation with a  $10\ \mu\text{m}$  wavelength was assumed. The probe-sample geometry, shown in Figure 2, results in scattering of IR radiation with the direction of maximum scattering opposite to the direction of incoming light in the plane parallel to the sample's surface and propagation at a grazing angle in the perpendicular plane (data not shown). This finding validates our choice of light collection geometry (Figure 1). In the calculations reported below, the numerical grid size was 50 nm, and the time step was chosen to satisfy a numerical stability criterion (for a cubic lattice with 50 nm spacing,  $\Delta t < 0.096$  fs). First, we calculated the infrared signal when the scattering probe scans over a rectangular block placed on the surface, maintaining a constant gap to the surface; this process simulates AFM imaging. Figure 9 shows calculations performed for a dielectric feature on the conductive surface with a relative permittivity equal to 2. The dielectric block size is  $1\ \mu\text{m} \times 0.5\ \mu\text{m} \times 0.25\ \mu\text{m}$ , and the probe (350 nm size) scans perpendicular to the longer axis of the block. To calculate the ac component of the infrared signal, intensities of scattered light, computed at different heights of conductive probe scanning, were subtracted, where the absolute values of the resulting signals represent the ac signals collected in our experiment.<sup>11</sup> The infrared signals shown in Figure 9 were

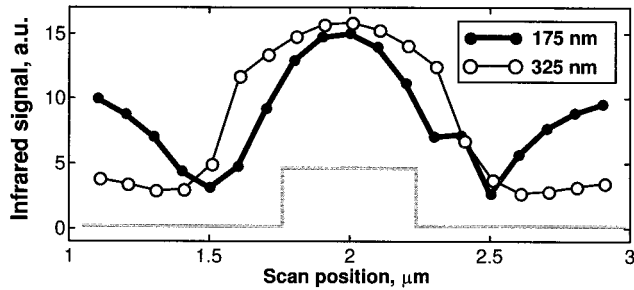


**Figure 9.** FDTD calculations of scattering from a dielectric object placed on a flat surface. These are constant-gap calculations of the probe scanning over a dielectric topographic feature placed on the surface of a conductor. See the text for the calculation parameters. The individual graphs correspond to different probe-sample separations, as indicated on the figure. The signal collected closer to the surface oscillates when it approaches a topographic feature. There is no such oscillation at larger distances; the signal exhibits steep transitions corresponding to the sharp motion that the probe makes to maintain a constant gap.

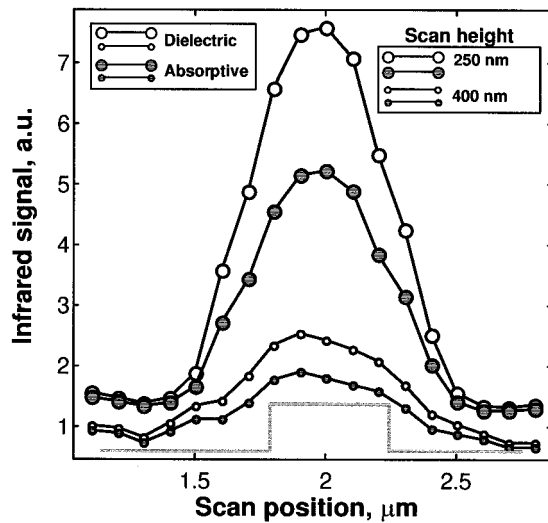


**Figure 10.** FDTD calculations of a constant-height scanning above dielectric and absorptive objects on the surface of a conductor. As the probe goes over the object, the signal changes slowly, with the transition distance increasing for larger probe separation from the surface. The infrared signal attenuation for an absorptive object is larger than for a bare layer of the same thickness. The magnitude of this attenuation variation depends on probe-surface distance. This effect can be used to enhance chemical contrast in near-field imaging.

calculated at mean heights of 175 and 325 nm above the surface. The shape of the block on the surface is shown below the plots. At a height of 175 nm, the resulting signal bears little resemblance to the shape of the object on the surface. Further away from the surface, the signal shape simplifies, but very sharp transitions ( $\sim 100$  nm) on the object sides indicate that the signal is greatly determined by probe motion.

The signal obtained while scanning above the surface at a constant height was calculated for a block of the same size as above, and the results are shown in Figure 10. Here, we calculated scattering for dielectric and Lorentzian materials.<sup>21</sup> The real part of the permittivity of the Lorentzian material was the same as for a dielectric; the absorption coefficient for this material was 300 mOD/ $\mu\text{m}$ . The signal calculated for the absorbing material is similar in shape to that of the dielectric material, with an obvious reduction in amplitude. The difference between dielectric and Lorentzian material signals does not simply relate to

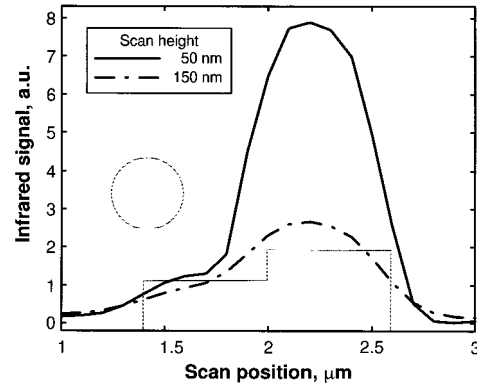


**Figure 11.** Effect of the sample topography on the infrared signal collected at a constant height. Variation of the signal from dielectric objects of different heights depends on the separation of the scanning plane from such objects.

absorption by the surface layer. For larger surface-sample separations, the apparent absorption coefficient is about twice as large as the Beer's law layer absorption, and for smaller separations the difference in absorption is even more significant, 3 times as large. We think that multiple scattering between the probe and the surface is responsible for this effect; the closer the probe is to the surface, the more important multiple scattering becomes.

We also conduct calculations to evaluate the effect of the sample geometry on an infrared signal collected at constant-height scanning. The calculations include two dielectric blocks with the same permittivity but different heights. The results are presented in Figure 11, along with a line indicating the profiles of the probe and the objects on the surface. Two different scan heights were considered: 50 and 150 nm. The calculations show that when one dielectric object is much closer to the scanning plane than the other, the resulting signal is dominated by the close object; this elucidates the origin of a signal above the topographic feature in constant-height mode (Figure 6). We also conclude that scanning at a constant height above the rough surface does not completely eliminate contrast related to the topography;<sup>23</sup> the topographic features in such scanning are merely getting smeared as the distance increases.

## Conclusions

We have performed scanning infrared near-field microscopy using an apertureless probe technique. The experimental data have been brought into reference with two basic models for the electromagnetics. The first model includes plane wave light scattering by a conductive sphere and an infinitely wide absorptive layer placed on a semi-infinite conductor. This model predicts dependence of the signal on the layer absorption and topographic coupling into the infrared signal resulting from constant-gap scanning. The model explains that experimental observations of nonmonotonic dependence of the scattered infrared signal on probe-sample distance are caused by interference phenomena. The experimental data also indicate that a significant component in the infrared contrast arises from the probe following topography. A method to minimize the influence of topography on the near-field signal has been demonstrated. A theoretical model based on a finite difference time domain method was used to calculate scattering from objects placed on a flat surface. Both constant tip-sample gap and constant tip-substrate height analyses were made. It was found that topography following results in the signal coupled to the probe motion and that constant-height imaging is a preferred mode of

operation. However, constant-height scanning does not completely eliminate contrast related to topography, as illustrated by experimental data and theoretical calculations. FDTD calculations also indicate that the infrared signal attenuation for an absorptive object is larger than for a bare layer of the same thickness. It appears that multiple scattering events can increase the attenuation of light underneath the scattering probe, leading to attenuation that does not scale simply with sample

thickness. This effect may be used to enhance chemical contrast in near-field imaging and will be the focus of a future report.

**Acknowledgment.** We gratefully acknowledge the Office of Naval Research (ONR N001-96-1-0735) and DARPA (DAAD16-99-C-1036) for support. B.A. acknowledges a Mellon predoctoral fellowship.

LA001401V